



## Research paper

Understanding the “seesaw effect” of interlayered K<sup>+</sup> with different structure in manganese oxides for the enhanced formaldehyde oxidationJinlong Wang<sup>a,b,1</sup>, Jun Li<sup>b,1</sup>, Pengyi Zhang<sup>a,c,\*</sup>, Gaoke Zhang<sup>b,\*\*</sup><sup>a</sup> State Key Joint Laboratory of Environment Simulation and Pollution Control, School of Environment, Tsinghua University, Beijing 100084, China<sup>b</sup> School of Resources and Environmental Engineering, Wuhan University of Technology, Wuhan 430070, China<sup>c</sup> Beijing Key Laboratory for Indoor Air Quality Evaluation and Control, Beijing 100084, China

## ARTICLE INFO

**Keywords:**  
 Layered MnO<sub>2</sub>  
 Formaldehyde  
 Potassium  
 Catalysis  
 Seesaw effect

## ABSTRACT

Although the potassium-promoted catalysts exhibit improved catalytic activities, the role of potassium with different structural sites still needs to be studied by more experiments and theory calculation. Herein, potassium (K<sup>+</sup>) formed via different binding sites (isolated and localized) over layered MnO<sub>2</sub> was investigated. The isolated K<sup>+</sup> dissociated between layers via weak chemical bond while localized K<sup>+</sup> coordinated with oxygen atoms at vacancy site. K<sup>+</sup> with localized type (L-MnO<sub>2</sub>) exhibited the higher activity and the lower E<sub>a</sub> (45.2 kJ/mol), compared with isolated one (58.1 kJ/mol) under 200 ppm HCHO, 120,000 mL/g h GHSV and ~45% relative humidity. Evidenced by diffuse reflectance infrared Fourier transform spectroscopy (DRIFTS), hydrogen temperature programmed reduction (H<sub>2</sub>-TPR) and density functional theory (DFT) simulation, the isolated K<sup>+</sup> in interlayer are energetically favourable for dissociation of O<sub>2</sub> as well as H<sub>2</sub>O by charge transfer from potassium to oxygen. As a result, the desorption of H<sub>2</sub>O was inhibited, thus, became the kinetic barriers during the whole reaction process. K<sup>+</sup> with localized form possessed suitable ability for O<sub>2</sub> activation and weak adsorption of H<sub>2</sub>O, exhibiting enhanced catalytic activity. Inspired by the seesaw effect, a clear understanding of K<sup>+</sup> effect on layered MnO<sub>2</sub> towards O<sub>2</sub> adsorption and H<sub>2</sub>O desorption was illustrated.

## 1. Introduction

Formaldehyde (HCHO) is one of the common indoor air pollutants. It mainly comes from the continuous release of decorating materials and furniture [1]. Besides, the generation of HCHO from outdoor photochemical reaction may also affect the quality of indoor air through the ventilation [2,3]. Long term exposure to the high concentration of HCHO will seriously damage the eye, nerve and respiratory system and even causes carcinogenic risk to human being [4]. Thus, the efficient abatement of HCHO is necessary for the improvement of indoor air quality. Among all the strategies that have been reported to eliminate indoor HCHO, heterogeneous catalysis has been highlighted as one of the most promising techniques, which can transform HCHO into harmless CO<sub>2</sub> and H<sub>2</sub>O with low energy consumption.

Supported noble metal catalysts showed great efficiency to decompose HCHO at low temperature. In 2005, Zhang et al. [5] first reported Pt/TiO<sub>2</sub> with high efficiency and stability for HCHO oxidation at room temperature, opening up a prospective way for HCHO removal. After

that, researchers focused on the effects of Pt species itself and supports to improve the activity [6–13]. In addition, Pd/Beta, Pd/TiO<sub>2</sub>, Pd/CeO<sub>2</sub>, Au/CeO<sub>2</sub>, Au/FeO<sub>x</sub>, Au/TiO<sub>2</sub>, Ag/MnO<sub>2</sub> etc. were also investigated for HCHO oxidation at low temperature [14–23]. Although noble metal catalysts exhibited high catalytic activity, more inexpensive catalysts were expected to be further investigated for wide use.

Transition metal oxides such as Co<sub>3</sub>O<sub>4</sub>, CeO<sub>2</sub>, FeO<sub>x</sub> were found to be active for HCHO oxidation [24–26]. In 2002, Sekine et al. [27] first compared the activity of different metal oxides (Ag<sub>2</sub>O, PdO, MnO<sub>2</sub>, CoO, TiO<sub>2</sub>, CeO<sub>2</sub> and Mn<sub>3</sub>O<sub>4</sub>) for HCHO conversion and found MnO<sub>2</sub> showed the best activity. Manganese oxides have a wide range of stoichiometry and exist in various crystal structures due to the special outer shell electronic structure (3d<sup>5</sup>4s<sup>2</sup>). Recently, many efforts have been made to improve the activity of manganese oxides for HCHO oxidation [28–36]. The activities of different crystal phase ( $\alpha$ -,  $\beta$ -,  $\gamma$ - and  $\delta$ -MnO<sub>2</sub> (i.e. birnessite)) were also compared and  $\delta$ -MnO<sub>2</sub> showed the best performance [37]. The potassium-containing layered  $\delta$ -MnO<sub>2</sub> has a two-dimensional structure formed by [MnO<sub>6</sub>] octahedral and

\* Corresponding author at: State Key Joint Laboratory of Environment Simulation and Pollution Control, School of Environment, Tsinghua University, Beijing 100084, China.

\*\* Corresponding author.

E-mail addresses: [zpy@tsinghua.edu.cn](mailto:zpy@tsinghua.edu.cn) (P. Zhang), [zgkww@126.com](mailto:zgkww@126.com) (G. Zhang).<sup>1</sup> These authors contributed equally to this work.

intercalated by  $K^+$  ion for charge balance.  $K^+$  ions associated with water molecules prevents collapse of the layer structure (Fig. S1). It is reported that layered  $MnO_2$  exhibited the activity for the complete decomposition of HCHO even at room temperatures, and its activity was also influenced by the content of water, interlayer cations and ultrathin layer structure [38–40]. To further improve its activity, necessary surface modifications are still needs to be investigated.

Recently, it has been reported that alkali-promoted catalysts exhibited enhanced catalytic activities. For examples, Hou et al. [41] found that the increased  $K^+$  concentration resulted in a considerable enhancement of lattice oxygen activity in OMS-2 nanorod. Similar promotion effects of alkali metals have also been observed in formaldehyde oxidation over hollandite manganese oxide [42,43]. The isolated potassium atoms anchored on the open-framework structure was hybridized d-sp orbitals that promoted oxygen activation. In addition, Zhang et al. [7] explained the role of  $K^+$  atoms from another point of view. The atomically dispersed  $Na\text{-Pt-O(OH)}_x$  species can activate  $H_2O$  effectively and catalyze the facile reaction between surface OH and formate species to total oxidation products. This phenomenon was also observed in  $K\text{-Ag-MnO}_2$  and  $Na\text{-Pd/TiO}_2$  catalysts [15,44]. According to the above analysis, it could be reasonably concluded that the addition of alkali metal could facilitate the activation of both chemisorbed oxygen and water. This phenomenon was also proved in the water-gas shift reaction, i.e. the electron-donor effect was theoretically predicted that electron-abundant potassium atoms are energetically favourable for the adsorption of  $O_2$  or  $H_2O$  [45]. In addition, the isolated K atoms anchored on the surface manganese oxide was also proved to be more negatively charged compared with  $K^+$  in potassium compounds, which was beneficial to  $O_2$  adsorption [43], and it was also proved for  $H_2O$  adsorption [45]. However, as for HCHO oxidation,  $O_2$  acts as a reactant and  $H_2O$  is a product. Note that the great contribution of electron-donor effect by  $K^+$ , the introduction of alkali metals may inhibit the desorption of  $H_2O$ , i.e., the product's desorption may become the kinetic barriers during the whole reaction process. Thus, the adsorption of  $O_2$  and the desorption of  $H_2O$  should be considered from the whole catalytic process (adsorption, reaction and desorption). Catalysts possess balanced ability for both  $O_2$  activation and  $H_2O$  desorption could exhibit enhanced catalytic activity. Thinking of the seesaw recreation, only if the weight of the kid loaded on each side was suitable, could they be enjoyable. Similarly, the ability for reactant adsorption and the ability for product desorption should be balanced.

Herein, we investigated the nature of the  $K^+$  promotion effect in HCHO oxidation process, aiming to figure out the role of  $K^+$  ions formed over layered  $MnO_2$  via different geometric structures (isolated or localized). The isolated  $K^+$  existed between layers for charge balance via weak chemical bond while localized  $K^+$  was anchored on the surface of layered  $MnO_2$  via vacancy effect reported in our previous research [39]. It was found that localized  $K^+$  on the surface of layered  $MnO_2$  exhibited higher catalytic activity for HCHO oxidation, benefited from the “seesaw effect” with suitable ability for both  $O_2$  adsorption and  $H_2O$  desorption, which was proved by DRIFTS,  $H_2\text{-TPR}$  and DFT calculation.

## 2. Experimental

### 2.1. Catalyst preparation

All chemicals used for sample preparation were of analytical grade.

#### 2.1.1. Synthesis of isolated $K^+$ type of $MnO_2$ ( $I\text{-MnO}_2$ )

$I\text{-MnO}_2$  was synthesized as follows: 1.0 g of  $KMnO_4$  and 0.15 g  $MnSO_4\text{H}_2O$  were dissolved into a beaker with 70 mL deionized water. After that, the solution was transformed into a hydrothermal reactor. The temperature was kept at 200 °C for 12 h. After the reactor was taken out and cooled down to room temperature. The final precipitate was centrifuged and washed 3 times to remove possible residual

impurities. Then, the precipitate was dried in an oven at 105 °C for 12 h. Finally, the sample was calcined in a muffle furnace at 300 °C for 3 h.

#### 2.1.2. Synthesis of localized $K^+$ type of $MnO_2$ ( $L\text{-MnO}_2$ )

$L\text{-MnO}_2$  was synthesized through “top-down” strategy (i.e., two procedures with first step for the generation of  $V_{Mn}$  and second step for the localization of  $K^+$ ). 0.4 g of synthesized  $I\text{-MnO}_2$  was immersed in the 100 mL solution of 1 M  $HNO_3$  for 6 h at room temperature (~25 °C) with continuous stirring to replace potassium ion and generate certain amount of manganese vacancy, which was explained in SI part (Fig. S2 and S3). Then the suspension was centrifuged and the precipitate was washed 3 times with deionized water. After that, the obtained sample was immersed in 100 mL of 1 M KOH solution for 6 h under continuous stirring followed by 3 times deionized water washing and 300 °C calcination.

For comparison, 0.4 g of synthesized  $I\text{-MnO}_2$  was immersed in the 100 mL solution of  $HNO_3$  (0.01 M, 0.1 M and 1 M) or KOH (1 M) for 6 h with continuous stirring. Then the suspension was centrifuged and the precipitate was washed 3 times with water and calcinated under 300 °C. Samples with solo acid treatment or base treatment were denoted as  $A\text{-MnO}_2$  and  $B\text{-MnO}_2$ , respectively.

### 2.2. Characterization

X-ray diffraction (XRD) analysis was carried out on a D8-Advance X-ray diffractometer (Bruker, Germany) using  $Cu K\alpha$  radiation ( $\lambda=0.1542$  nm). Transmission electron microscopy (TEM) analysis was conducted on a JEOL 2011 transmission electron microscope (JEOL, Japan) with an accelerating voltage of 150 kV. X-ray photoelectron spectroscopy (XPS) analysis was conducted on a ESCALAB 250Xi X-ray photoelectron spectrometer (Thermo Fisher, USA) operated at a pass energy of 30 eV, using  $Al K\alpha$  ( $\lambda=1486.7$  eV) as an exciting X-ray source. Nitrogen adsorption-desorption experiments were carried out on an automated surface and pore size analyser (Quantachrome, USA). Samples were degassed in vacuum at 200 °C for 4 h before the measurement. Thermal gravity analysis (TGA) was conducted on TGA/DSC 1 STARe (Mettler Toledo, Switzerland). The temperature was increased by 10 °C/min from 30 °C to 500 °C. Raman spectra was recorded on an inVis (Renishaw, U.K.) with the 532 nm wavelength excitation laser source. Hydrogen temperature programmed reduction ( $H_2\text{-TPR}$ ) was performed on an AutoChem 2920 adsorption instrument (Micromeritics, USA) with TCD detector. The temperature was increased by 5 °C/min from 40 °C to 500 °C under  $H_2$  (5%  $H_2/Ar$ ) atmosphere with a flow rate of 50 mL/min. DRIFTS was carried out on a NICOLET 6700 FTIR spectrometer (Micromeritics, USA). The time-resolved spectra were then obtained by 32 scans at a resolution of 4  $cm^{-1}$  at room temperature. Samples were pretreated by  $N_2$  for 30 min under room temperature before exposing to HCHO containing gas (~80 ppm at a flow rate of 30 mL/min balanced by pressured oxygen). DFT calculations were performed by CASTEP package on the basis of the plane-wave-pseudo-potential approach. More details about DFT calculation were described in Supplementary Information (SI).

### 2.3. Catalytic activity test

HCHO removal activity of various  $MnO_2$  was tested in a fixed bed flow reactor. 100 mg of  $MnO_2$  with 40/60 meshes was filled in a quartz tube reactor. The gas stream was mixed with dry air, wet air and HCHO gas. The relative humidity was controlled at the level of ~45% and the inlet concentration of HCHO was controlled at ~200 ppm. The total flow rate was 200 mL/min and the corresponding gas hourly space velocity (GHSV) was 120 L/g h. The activity of  $MnO_2$  was tested under temperatures ranging from 30 °C to 150 °C. The inlet concentration of HCHO was determined by MBTH method [38]. The ratio of HCHO conversion was calculated according to the generation of  $CO_2$ , which

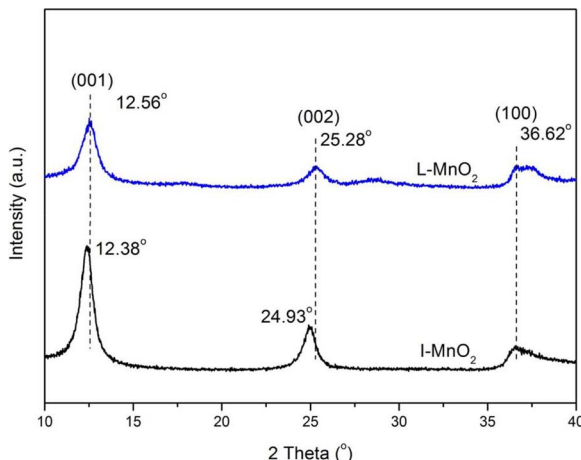


**Fig. 1.** High-resolution XRD patterns of I-MnO<sub>2</sub> and L-MnO<sub>2</sub> samples scanning from 10° to 40°.

was determined by a GC-2014 gas chromatograph (Shimadzu, Japan) equipped with a methanizer and a flame ionization detector (FID). No carbon products other than CO<sub>2</sub> were detected. To calculate the apparent activation energy (E<sub>a</sub>), the ratio of HCHO conversion was controlled below 15% and the corresponding GHSV was varied from 60 to 240 L/g h.

### 3. Results and discussion

#### 3.1. Phase structures and morphology

The XRD patterns are illustrated in Fig. 1, peaks located around 12.3°, 24.6° and 36.5° are the characteristic 2θ diffraction peaks of layered MnO<sub>2</sub>. The position of (001) and (002) crystal facet was used to estimate the layer distance (Fig. 1). As for the I-MnO<sub>2</sub> sample, the 2θ of (001) and (002) diffraction positions were 12.38° and 24.93°, respectively. However, as for L-MnO<sub>2</sub> sample, the 2θ of (001) and (002) diffraction positions shifted to the higher angles (12.56° and 25.28°), indicating the shrinkage of interlayer spacing. Based on the shift of (001) reflection, the interlayer spacing changed from 7.15 to 7.05 Å, which might be caused by different binding site of interlayered K<sup>+</sup>. Furthermore, no such variation was observed for the (100) reflection, indicating the stability of [MnO<sub>6</sub>] slab.

Fig. 2 shows the TEM images of the I-MnO<sub>2</sub> and L-MnO<sub>2</sub> sample. The I-MnO<sub>2</sub> exhibited flower-like nanospheres consisting of nanosheets (Fig. 2a). And the L-MnO<sub>2</sub> sample also showed flower-like structure (Fig. 2b). Thus, it means the sequent acid and basic treatment did not affect the major morphology of original I-MnO<sub>2</sub>. However, the high resolution TEM images showed some differences. Viewing from the {001}, the lattice fringe spacing was 0.24 nm, corresponding to the interspace between two (100) planes of layered-structure MnO<sub>2</sub> (Fig. 2c). The clear lattice orientation demonstrated that the I-MnO<sub>2</sub> sample was well crystallized. As for the L-MnO<sub>2</sub> sample (Fig. 2d), the lattice fringe in some parts became fuzzy and discrete, which could be ascribed to the formation of V<sub>Mn</sub> and localization of K<sup>+</sup> close to the V<sub>Mn</sub> site.

The N<sub>2</sub> adsorption-desorption isotherms was shown in Fig. S4. The adsorption isotherms belong to type IV, indicating the presence of interconnected mesopores with some constrictions. In the pore-size distribution curves (inset in Fig. S4) of I-MnO<sub>2</sub> and L-MnO<sub>2</sub>, peaks occurred at ca. 4.7 and 3.9 nm, respectively, confirming the meso-porosity of the catalysts. It is well known the aggregation of nanoflakes may form the slit pores. As listed in Table 1, the specific surface area of original I-MnO<sub>2</sub> sample was 68.3 m<sup>2</sup>/g, that of L-MnO<sub>2</sub> was a little higher (88.0 m<sup>2</sup>/g). For comparison, the specific surface area of A-MnO<sub>2</sub> was also measured, which was up to 96.3 m<sup>2</sup>/g.

#### 3.2. Surface chemical state

The surface element content detected by XPS was summarized in Table 2. As for I-MnO<sub>2</sub>, the molar ratio of K/Mn and Mn/O is 0.46 and 0.50, respectively. As for L-MnO<sub>2</sub>, the K/Mn molar ratio slightly increased to 0.51. The ICP-AES analysis also gave a similar result (Table 1). The Mn/O molar ratio decreased to 0.43 (smaller than the stoichiometric ratio 0.5), indicating the absence of Mn atoms.

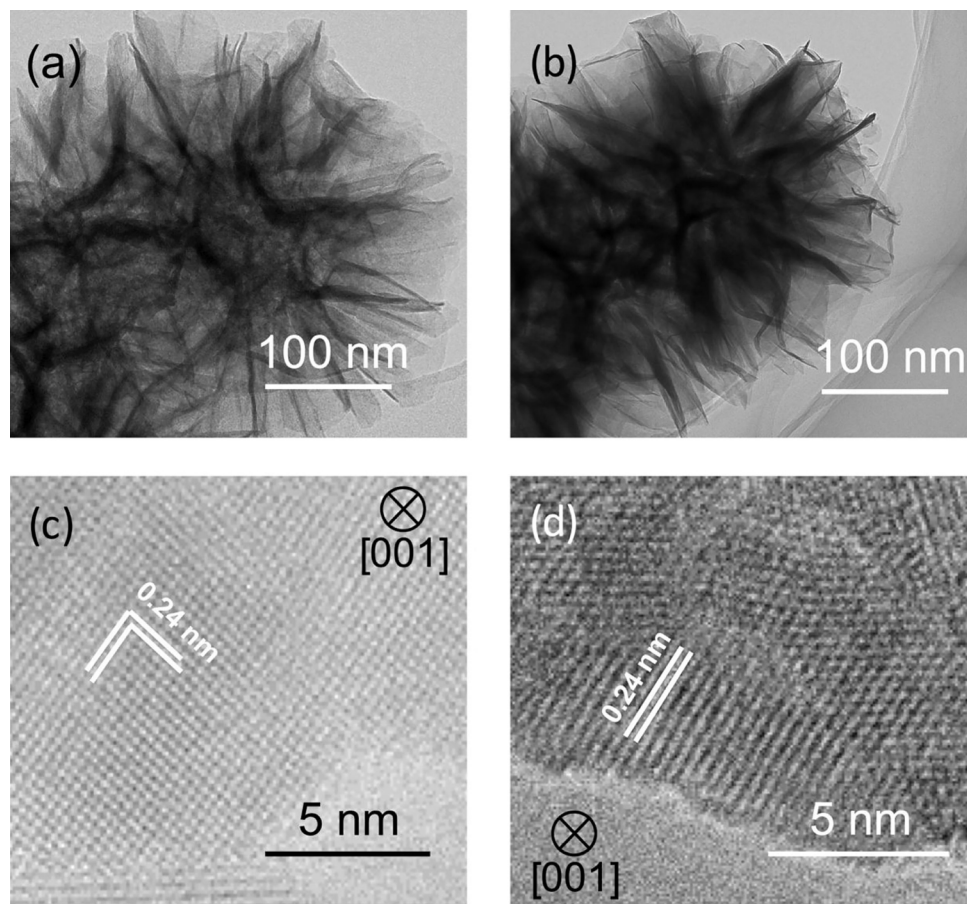
Fig. 3a displays the Mn 2p spectra of the I-MnO<sub>2</sub> and L-MnO<sub>2</sub> sample. The Mn 2p<sub>3/2</sub> spectra was deconvoluted into two peaks with binding energy at 641.7 and 642.9 eV, which is ascribed to Mn<sup>3+</sup> and Mn<sup>4+</sup>, respectively [39,46]. No Mn<sup>2+</sup> species were detected by XPS. The quantitative analysis on the molar ratios of surface Mn<sup>3+</sup>/Mn<sup>4+</sup> was summarized in Table 2. The molar ratio of Mn<sup>3+</sup>/Mn<sup>4+</sup> of the L-MnO<sub>2</sub> (2.58) was much higher than that of the I-MnO<sub>2</sub> (1.14) sample, which could be explained that localized K<sup>+</sup> at vacancy site of [MnO<sub>6</sub>] slab had a strong interaction with O, weakening the Mn-O bond. As a result, the chargeability of Mn atoms increased, and the content of Mn<sup>3+</sup> accordingly increased.

Fig. 3b shows the O 1s spectra of the I-MnO<sub>2</sub> and L-MnO<sub>2</sub> sample. The peaks at the binding energy of 529.7–530.3 eV, 531.4–531.8 eV and 532.9–533.7 eV, corresponded to lattice oxygen (O<sub>latt</sub>), surface adsorbed oxygen species (O<sub>ads</sub>) and surface residual water, respectively [39,46]. The binding energy of O<sub>latt</sub> in the I-MnO<sub>2</sub> located at 530.0 eV, while it was 529.9 eV in the L-MnO<sub>2</sub> sample. The molar ratio of O<sub>ads</sub>/O<sub>latt</sub> was also calculated as shown in Table 2, it was 0.15 for I-MnO<sub>2</sub> and 0.10 for L-MnO<sub>2</sub>, respectively. This result suggests that I-MnO<sub>2</sub> owned more abundant surface adsorbed oxygen species. This can be ascribed to the existence of different type of K<sup>+</sup>, which would be discussed below.

The K 2p spectra are displayed in Fig. 3c. The binding energy of the K 2p peak shifted to lower value for I-MnO<sub>2</sub> (292.6 eV) with respect to that of L-MnO<sub>2</sub> (292.8 eV), which means the localized K<sup>+</sup> exhibited lower electron density compared with the isolated one. Similar effect has also been observed in hollandite manganese oxide [42,43]. A theoretical calculation indicates that the electron-abundant potassium atoms are energetically favourable for dissociation of O<sub>2</sub> by charge transfer from potassium to O<sub>2</sub> [43]. As a result, easier dissociative adsorption of O<sub>2</sub> could account for higher content of O<sub>ads</sub> species in the I-MnO<sub>2</sub> sample illustrated by the XPS analysis.

For better understanding the function of localized K<sup>+</sup> on [MnO<sub>6</sub>] slab, the A-MnO<sub>2</sub> sample was also characterized by XPS (Fig. S5). The K/Mn ratio was as low as 0.04. And the Mn/O atomic ratio was 0.38, which was much smaller than the stoichiometric ratio of MnO<sub>2</sub> (0.5), indicating the presence of V<sub>Mn</sub>. In addition, the A-MnO<sub>2</sub> showed the lowest surface Mn<sup>3+</sup>/Mn<sup>4+</sup> molar ratio (0.23) (Fig. S5a), which confirmed the assumption that the disproportionation of Mn<sup>3+</sup> into Mn<sup>4+</sup> and dissolved Mn<sup>2+</sup> happened during acid treatment, resulting in low content of Mn<sup>3+</sup>. The binding energy of O<sub>latt</sub> located at 530.3 eV (Fig. S5b), which was much higher than that of L-MnO<sub>2</sub> sample. This means the electron density of oxygen was reduced due to the introduction of V<sub>Mn</sub>.

Raman spectra of I-MnO<sub>2</sub> and L-MnO<sub>2</sub> are shown in Fig. 3d. Three major peaks centred around 600 cm<sup>-1</sup> can be assigned to typical layered MnO<sub>2</sub>, which could be regarded as the symmetric stretching vibration  $\nu_2(\text{Mn}-\text{O})$  of [MnO<sub>6</sub>] groups,  $\nu_3(\text{Mn}-\text{O})$  stretching vibration and the stretching vibration of Mn-O-Mn varying from high to low wavenumber [47]. The general similarity of the spectrum suggested that I-MnO<sub>2</sub> and L-MnO<sub>2</sub> had the same basic structure. However, all peaks in L-MnO<sub>2</sub> exhibited red shift to lower wavelength, indicating lattice distortion or residual stress occurred. In addition, two bands at 281 and 406 cm<sup>-1</sup> showed rather weak intensity, which could be ascribed to weak bonding for the cations (K<sup>+</sup> in this case) in the I-MnO<sub>2</sub> interlayers [47]. However, no obvious peak could be observed on L-MnO<sub>2</sub>, further indicating the location of K<sup>+</sup> in L-MnO<sub>2</sub> was different from that in I-MnO<sub>2</sub>.



**Fig. 2.** TEM images of low and high magnification of (a), (c) I-MnO<sub>2</sub>; (b), (d) L-MnO<sub>2</sub>.

**Table 1**  
Physical properties of different samples.

Sample	S <sub>BET</sub> (m <sup>2</sup> /g)	Pore volume (cm <sup>3</sup> /g)	Pore diameter (nm)	K/Mn <sup>a</sup>	Interlayer distance (Å) <sup>b</sup>
I-MnO <sub>2</sub>	68.3	0.24	14.8	0.41:1	0.715
A-MnO <sub>2</sub>	96.3	0.30	13.7	0.03:1	0.729
L-MnO <sub>2</sub>	88.0	0.26	12.6	0.44:1	0.705

<sup>a</sup> Obtained from EDS analysis.

<sup>b</sup> Obtained from XRD analysis.

**Table 2**  
Surface chemical compositions of analyzed by XPS.

Sample	Surface element content(at.%)			Molar ratios			
	K	Mn	O	K/Mn	Mn/O	Mn <sup>3+</sup> / Mn <sup>4+</sup>	O <sub>ads</sub> /O <sub>latt</sub>
I-MnO <sub>2</sub>	13.2	28.9	57.8	0.46	0.50	1.14	0.15
A-MnO <sub>2</sub>	1.1	27.3	71.6	0.04	0.38	0.23	0.07
L-MnO <sub>2</sub>	13.1	25.8	61.1	0.51	0.43	2.58	0.10

### 3.3. Evaluation of HCHO removal activity

Fig. 4a shows the catalytic performance of different samples for HCHO oxidation. The conversion of HCHO were increased with the rise of reaction temperature. T<sub>50</sub> and T<sub>90</sub> (corresponding to 50% and 90% HCHO conversion, respectively) were used to evaluate the activity of samples. As can be seen in Table 3, the values of T<sub>50</sub> for I-MnO<sub>2</sub> and L-MnO<sub>2</sub> are 107 and 76 °C, meanwhile, T<sub>90</sub> are 131 and 98 °C, respectively. For comparison, the catalytic activity of A-MnO<sub>2</sub> and B-MnO<sub>2</sub> was also detected. The activity of different samples followed the order:

L-MnO<sub>2</sub> > I-MnO<sub>2</sub> ≈ B-MnO<sub>2</sub> > A-MnO<sub>2</sub>. The activity of B-MnO<sub>2</sub> seemed unchanged compared with that of I-MnO<sub>2</sub> sample. It could be concluded that solo KOH treatment did not changed the structure of I-MnO<sub>2</sub> sample. In addition, the specific HCHO reaction rates (per unit surface area of catalyst) at 100 °C were compared. As can be seen from Table 3, the value of specific HCHO reaction rates for I-MnO<sub>2</sub>, A-MnO<sub>2</sub>, and L-MnO<sub>2</sub> were 0.09, 0.01, and 0.19 μmol/m<sup>2</sup> min, respectively. Besides, the apparent activation energy (E<sub>a</sub>) was also calculated according to Arrhenius plots for different samples (Fig. 4b). The value of E<sub>a</sub> for I-MnO<sub>2</sub>, A-MnO<sub>2</sub>, and L-MnO<sub>2</sub> were 58.1, 88.1, and 45.2 kJ/mol, respectively, which means HCHO was most easily oxidized by L-MnO<sub>2</sub>. As mentioned above, when I-MnO<sub>2</sub> suffered from acid treatment, V<sub>Mn</sub> simultaneously occurred with the leaching of K<sup>+</sup>, which inhibited the activity of surface oxygen. As a result, A-MnO<sub>2</sub> showed the worse performance than I-MnO<sub>2</sub>. The different activity of I-MnO<sub>2</sub> and L-MnO<sub>2</sub> might be resulted from their different location of K<sup>+</sup> in layered structure. Furthermore, the effect of gas hourly space velocity (GHSV) varying from 60,000 to 240,000 mL/g h was evaluated (Fig. 4c). Higher GHSV value would inhibit the whole formaldehyde oxidation process. The stability of L-MnO<sub>2</sub> for HCHO oxidation was also evaluated (Fig. 4d). The result of this continuous test (200 ppm of HCHO, 60000 mL/g h of GHSV, ~45% of relative humidity) illustrated that the removal efficiency of HCHO maintained at ~85% within 12 h at 80 °C, indicating the good stability for the elimination of HCHO.

### 3.4. The role of interlayered K<sup>+</sup> with different structure

The introduction of K<sup>+</sup> could change the local surface electronic structure of the layered MnO<sub>2</sub> and further tuned the binding strength of the reactant molecules. Herein, the adsorption energies of O<sub>2</sub> and H<sub>2</sub>O (E<sub>O2</sub> and E<sub>H2O</sub>) over different surface structure were calculated (Fig. 5). The adsorption energy of O<sub>2</sub> and H<sub>2</sub>O on I-MnO<sub>2</sub> was calculated to be

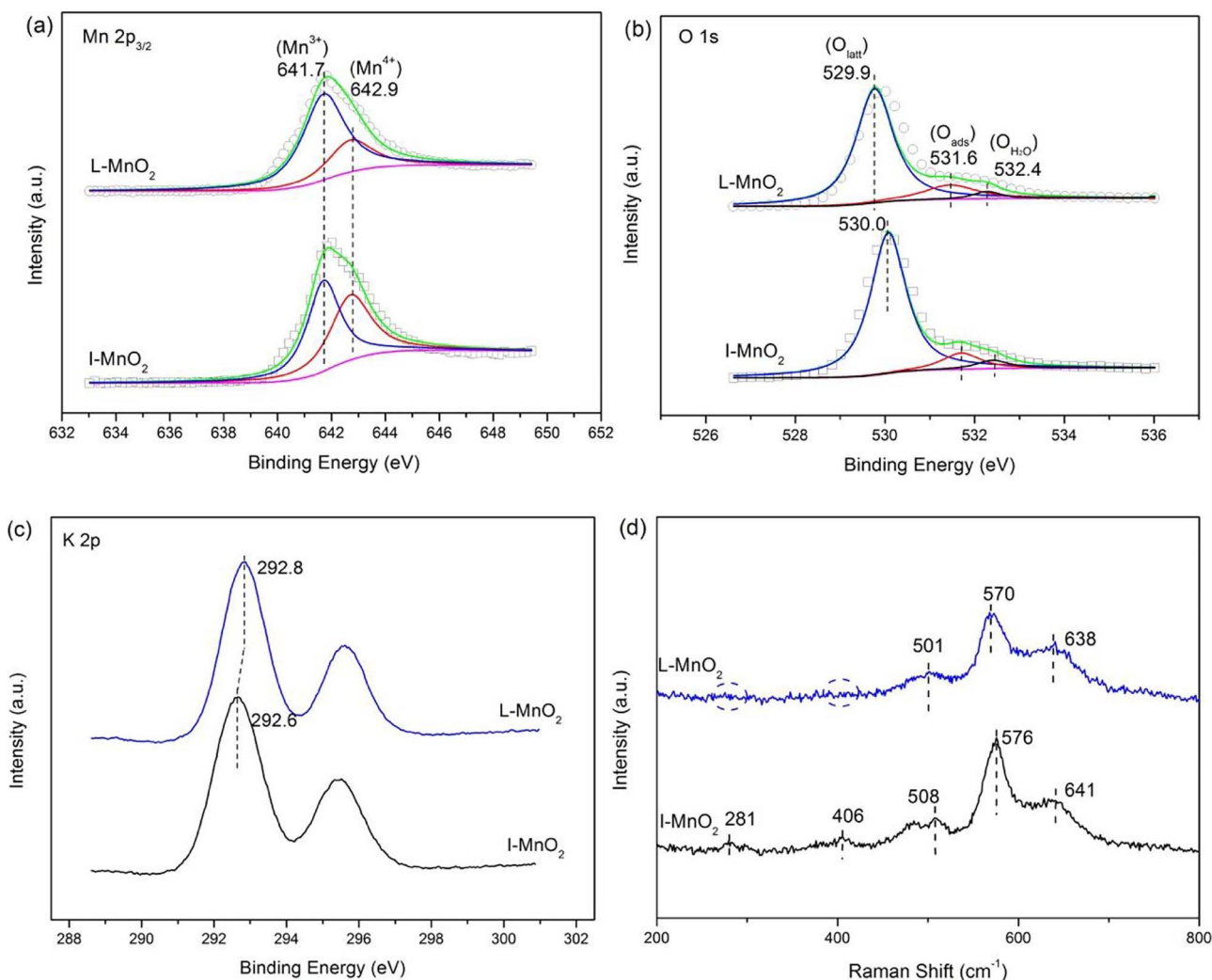


Fig. 3. (a) Mn 2p<sub>3/2</sub>, (b) O 1s, (c) K 2p XPS spectra and (d) Raman patterns of I-MnO<sub>2</sub> and L-MnO<sub>2</sub> samples.

0.29 and 1.2 eV, respectively. The low adsorption energy indicated that O<sub>2</sub> and H<sub>2</sub>O could be easily adsorbed and activated. The isolated K<sup>+</sup> in the middle of the layers are energetically favourable for dissociation of O<sub>2</sub>/H<sub>2</sub>O by charge transfer from potassium to oxygen. Similar phenomenon also occurred over hollandite manganese oxide [43]. The local transfer of sp electrons to empty d shell weakens the Pauli repulsion and allows the oxygen atom to approach and continue into the chemisorption region [43]. The easy adsorption of O<sub>2</sub>/H<sub>2</sub>O was favourable for the generation of surface hydroxyl and active oxygen species (surface hydroxyl could be formed via the dissociation of water molecules on unsaturated site or some reactions between chemisorbed O<sub>2</sub> and protons from H<sub>2</sub>O [48]; surface chemisorbed O<sub>2</sub> can accept delocalized electrons to form active oxygen species, such as O<sub>2</sub><sup>−</sup> and O<sub>2</sub><sup>2−</sup> [49]), which was beneficial to HCHO oxidation. However, as for HCHO oxidation, O<sub>2</sub> was as a reactant and H<sub>2</sub>O was a product, too much amount of water adsorbed on the surface of sample would in turn inhibit the whole reaction process due to the hard desorption of generated H<sub>2</sub>O. At this point, the desorption of water became the rate-limiting step [34]. In addition, adsorption energy of O<sub>2</sub> and H<sub>2</sub>O on [MnO<sub>6</sub>] slab over I-MnO<sub>2</sub> sample was also calculated (Fig. S6). The saturated six coordination Mn was not beneficial to the adsorption of O<sub>2</sub> (1.45 eV) and H<sub>2</sub>O (1.57 eV). Considering the interlayer distance (0.7 nm) and the size of formaldehyde molecular (0.44 nm), the K was selected as adsorption site rather than surface Mn over I-MnO<sub>2</sub> and L-MnO<sub>2</sub> sample. The adsorption energy of O<sub>2</sub> and H<sub>2</sub>O on A-MnO<sub>2</sub> was calculated to be 1.42 and −1.99 eV (Fig. S7), indicating a weak O<sub>2</sub>

adsorption and a strong H<sub>2</sub>O adsorption. As for A-MnO<sub>2</sub>, K<sup>+</sup> was extracted and the Mn on the {001} layer was saturated, which led to the weak bonding connection between Mn and O<sub>2</sub> molecular. However, the oxygen around V<sub>Mn</sub> site was not fully coordinated, which can be combined with H<sub>2</sub>O via H and O bonding. As for L-MnO<sub>2</sub>, K<sup>+</sup> ions coordinated with oxygen atoms at vacancy site that maximized the interactions with the support surface in order to minimize the total energy of the system. The O<sub>2</sub> adsorption energy over L-MnO<sub>2</sub> was calculated to be 0.82 eV, higher than I-MnO<sub>2</sub> (0.29 eV), similar to the H<sub>2</sub>O adsorption energy (5.79–1.2 eV). When K<sup>+</sup> was localized on the V<sub>Mn</sub> site, the localized potassium atoms have lower electron density than isolated ones (evidenced by XPS result), which weaken the electron transfer from potassium to oxygen. The adsorption of O<sub>2</sub> was suppressed, however, the desorption of H<sub>2</sub>O was enhanced, which in turn facilitated the whole reaction process.

The H<sub>2</sub>-TPR analysis was performed to determine the reducibility of the catalysts. As shown in Fig. 6, two main peaks were both observed on I-MnO<sub>2</sub> and L-MnO<sub>2</sub> samples, corresponding to the continuous reduction process of K<sub>x</sub>MnO<sub>2</sub> → Mn<sub>2</sub>O<sub>3</sub> → Mn<sub>3</sub>O<sub>4</sub> → MnO. The first main peak of the I-MnO<sub>2</sub> sample centred at 255 °C, while that of the L-MnO<sub>2</sub> sample shifted to higher temperature (270 °C), which indicated that the lattice oxygen (O<sup>2−</sup>) in the L-MnO<sub>2</sub> sample was less active. The strong bonding between the localized K<sup>+</sup> with the surface unsaturated O might inhibit the reactivity of surface oxygen. In addition, the surface lattice oxygen was more negative charged on L-MnO<sub>2</sub>, as evidenced by XPS O 1s result. It was also reported that lattice oxygen with lower

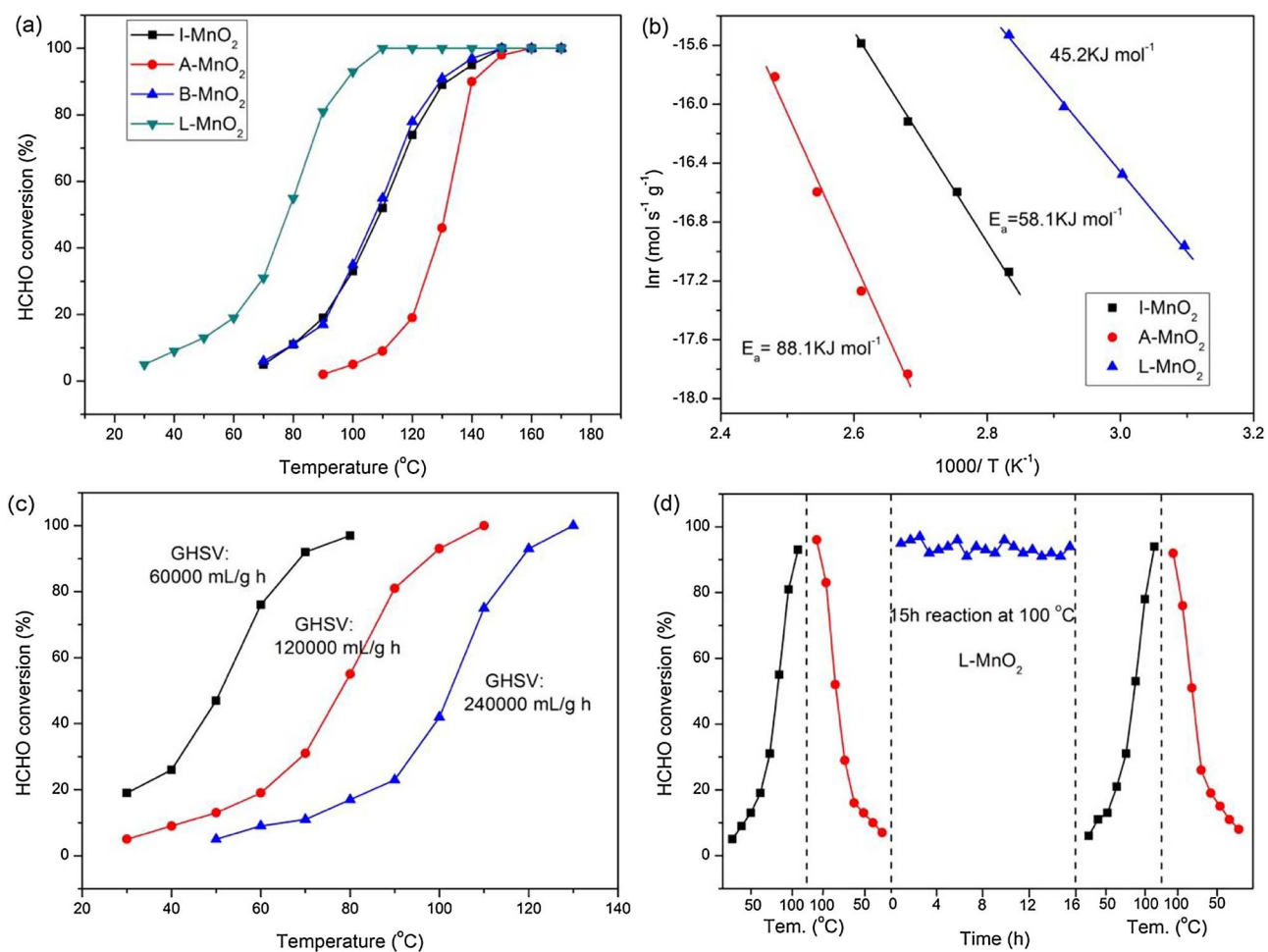


Fig. 4. (a) Activity profiles, (b) Arrhenius plots of the three samples, (c) effect of GHSV on the catalytic activity over L-MnO<sub>2</sub> and (d) stability of L-MnO<sub>2</sub>.

Table 3  
HCHO oxidation activity and apparent activation energies ( $E_a$ ) of different samples.

Sample	Catalytic activity (°C)	Rate at 100 °C (μmol/min)	Specific rate at 100 °C (μmol/ m <sup>2</sup> min)	Apparent activation energy (kJ/mol)
	T <sub>50</sub>	T <sub>90</sub>		
I-MnO <sub>2</sub>	107	131	0.61	58.1
A-MnO <sub>2</sub>	131	140	0.09	88.1
B-MnO <sub>2</sub>	105	128	0.09	—
L-MnO <sub>2</sub>	76	98	1.64	45.2

electronic density were more likely to accept electrons from the reactant [21]. The MvK mechanism involves two steps: the consumption of surface active lattice oxygen; the activation of gaseous oxygen to replenish the surface oxygen defects [50]. Here, isolated-type K<sup>+</sup> also facilitated the activation of the surface lattice oxygen. Similar phenomenon was also reported in Ag/HMO sample, isolated Ag in HMO showed high electronic density state, facilitating activation of both lattice oxygen and gaseous oxygen [20]. In addition, the H<sub>2</sub>-TPR analysis of A-MnO<sub>2</sub> was also conducted, the increase of main reduction peak (280 °C) as well as shoulder starting peak indicated the decreased catalytic activity.

HCHO was easily oxidized into CO<sub>2</sub> due to its simple structure once the reaction temperature was high. Herein, the in situ DRIFTS was conducted to clarify the intermediate species during HCHO oxidation at room temperature (Fig. 7). When samples were exposed to formaldehyde, peaks located at 1338, 1383, 1595/1546 and 2781–2967 cm<sup>-1</sup> were observed in all samples, which are assigned to

$\nu_s(\text{COO})$ ,  $\nu(\text{CH})$ ,  $\nu_{as}(\text{COO})$  and  $\nu(\text{CH})$  of formate (HCOO<sup>-</sup>) species [30,39], respectively. Formate species were easily formed on manganese oxides. As for I-MnO<sub>2</sub>, the generation of CO<sub>2</sub> located at 2316 cm<sup>-1</sup> was observed, indicating formaldehyde could be fully oxidized. However, the CO<sub>2</sub> intensity was relatively weak which could be explained by the weak adsorption ability on the surface of layered MnO<sub>2</sub> [34]. Dioxymethylene (DOM) species located at 1420 cm<sup>-1</sup> were also detected [39]. The peak of DOM was relatively low, which indicated that DOM species were more quickly converted. In addition, surface hydroxyl (-OH) located at 3592 cm<sup>-1</sup> was deceased with the increase of reaction time, which can be explained that -OH was participated in the reaction and was consumed during formate oxidation [7]. The wide range of bulging peak around 3100–3500 cm<sup>-1</sup> indicated that the generated H<sub>2</sub>O via formaldehyde oxidation was not easily desorbed. To further prove the adverse influence of adsorbed water, we compared the HCHO decomposition over the pristine I-MnO<sub>2</sub> and the I-MnO<sub>2</sub> after 24 h exposure to water vapor (I-MnO<sub>2</sub>-H<sub>2</sub>O). As shown in Fig. S8, the existence of H<sub>2</sub>O facilitated the HCHO adsorption via hydrogen bonding. However, too much amount of adsorbed water would occupy the active site, which inhibited the activation of O<sub>2</sub>, leading to the lower generation of CO<sub>2</sub>. It could be concluded that too much amount of water adsorbed on the surface of sample would inhibit the whole reaction due to its hard desorption.

In comparison, only CO located at 2179 cm<sup>-1</sup> was observed with no consumption of surface -OH over A-MnO<sub>2</sub>, indicating that O<sub>2</sub> was not easily activated (i.e. the surface O<sub>2</sub> adsorption energy is low). HCHO easily forms DOM species in the presence of oxygen. The sharp peak of DOM species dominated in the whole spectrum, which meant that they were not easily transformed to formate species due to the weak

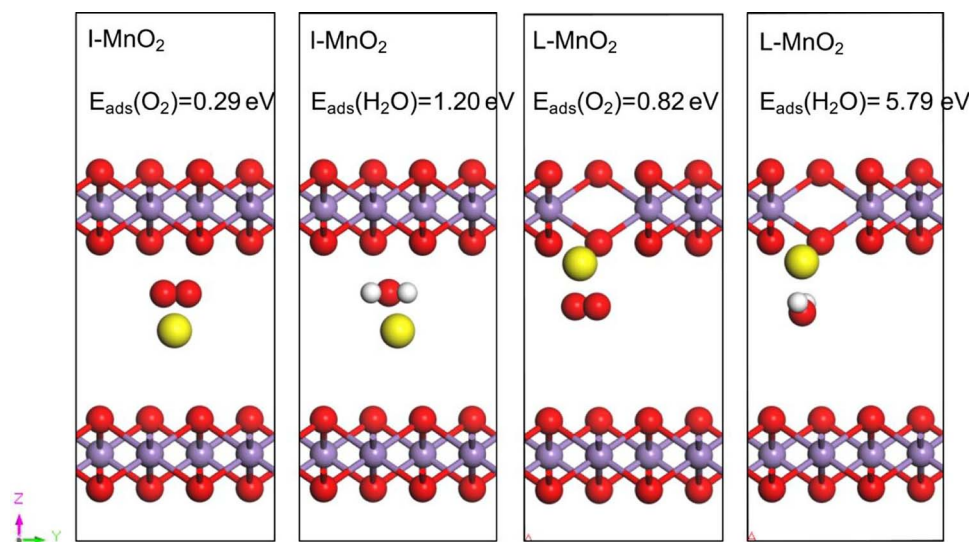


**Fig. 5.** The adsorption energy of O<sub>2</sub> and H<sub>2</sub>O over I-MnO<sub>2</sub> and L-MnO<sub>2</sub>. The adsorption site was selected at K site. The red, purple, yellow and grey spheres represent O, Mn, K and H atoms. (For interpretation of the references to colour in this figure legend, the reader is referred to the web version of this article.)

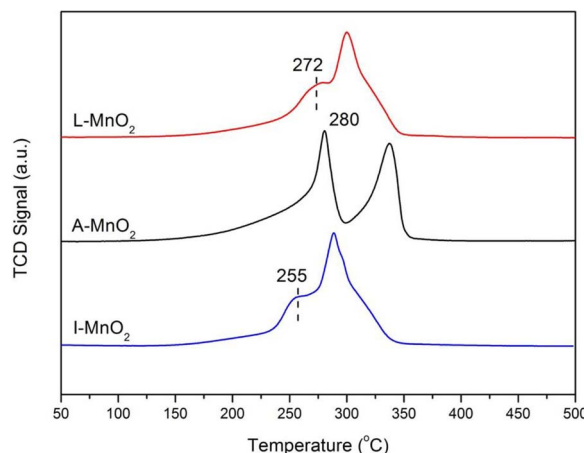


**Fig. 6.** H<sub>2</sub>-TPR analysis of different samples (I-MnO<sub>2</sub>, A-MnO<sub>2</sub> and L-MnO<sub>2</sub>).

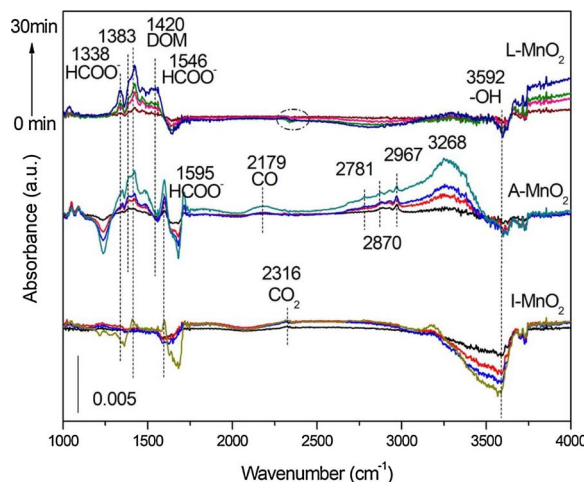


**Fig. 7.** In-situ DRIFTS of I-MnO<sub>2</sub>, A-MnO<sub>2</sub> and L-MnO<sub>2</sub> samples exposed to the flow of HCHO/O<sub>2</sub> at room temperature.

oxidation ability over A-MnO<sub>2</sub> catalyst. In addition, there was a wide peak around 3200 cm<sup>-1</sup>, indicating H<sub>2</sub>O was easily adsorbed on the surface of V<sub>Mn</sub> site, which was also proved by the calculation of H<sub>2</sub>O surface adsorption energy (-1.99 eV). The weak O<sub>2</sub> adsorption ability of A-MnO<sub>2</sub> as well as its hydrophilic characteristics together suppressed

the whole formaldehyde reaction process. When K<sup>+</sup> was localized on the V<sub>Mn</sub> site, only the CO<sub>2</sub> was observed with no CO detection, indicating a more effective pathway for the direct oxidation of surface formate compared with A-MnO<sub>2</sub> sample. In addition, DOM species were also observed, which followed the order: A-MnO<sub>2</sub> > L-MnO<sub>2</sub> > I-MnO<sub>2</sub>, indicating that localized K<sup>+</sup> showed lower HCHO oxidation ability than the isolated one. However, the wide range of relatively flat peak around 3100–3500 cm<sup>-1</sup> was observed, indicating that the generated H<sub>2</sub>O from HCHO oxidation was easily desorbed from catalysts.

The character of water adsorption over I-MnO<sub>2</sub>, A-MnO<sub>2</sub> and L-MnO<sub>2</sub> were also analyzed by TG analysis (Fig. S8). There were three stages of weight loss, corresponding to the desorption of physical water, chemical water and surface -OH, which were desorbed with the rise of temperature sequentially [38]. The initial two segments were used to estimate the content of adsorbed water, following the order: A-MnO<sub>2</sub> (13.4%) > I-MnO<sub>2</sub> (9.5%) > L-MnO<sub>2</sub> (8.6%), which was consistent with the DRIFTS result.

On the basis of the above discussion, two kinds of K<sup>+</sup> ions (isolated or localized) existed over layered MnO<sub>2</sub>, and their different effects on HCHO decomposition over layered MnO<sub>2</sub> were clearly illustrated. It is well known that simultaneous adsorption of O<sub>2</sub> for activation and desorption of H<sub>2</sub>O for sustainable reaction are an integral part in formaldehyde oxidation process. Like the structure of seesaw, the ability of O<sub>2</sub> (reactant) adsorption and H<sub>2</sub>O (resultant) desorption needs to be balanced. K<sup>+</sup> in the isolated form exhibited higher electronic density states, facilitating the adsorption of O<sub>2</sub> as well as H<sub>2</sub>O. As a result, the desorption of H<sub>2</sub>O became the kinetic barriers during the whole reaction process. However, K<sup>+</sup> in the localized form on [MnO<sub>6</sub>] slab possesses suitable ability for both O<sub>2</sub> activation and weak adsorption of H<sub>2</sub>O, thus exhibiting enhanced formaldehyde catalytic oxidation ability.

#### 4. Conclusion

In summary, the role of interlayered K<sup>+</sup> with different structure (isolated and localized) in manganese oxides for the enhanced formaldehyde oxidation was investigated. The isolated K<sup>+</sup> in interlayer are energetically favourable for dissociation of O<sub>2</sub> as well as H<sub>2</sub>O by charge transfer from potassium to oxygen atom. Even though the O<sub>2</sub> was activated, the desorption of H<sub>2</sub>O was inhibited, thus, became the kinetic barriers during formaldehyde oxidation process. K<sup>+</sup> with localized form possessed suitable ability for O<sub>2</sub> activation and weak adsorption of H<sub>2</sub>O, exhibiting enhanced catalytic activity. This finding gives evidence for the understanding of the function of K<sup>+</sup> promoters from the perspective of thermodynamics and dynamics, shedding light in

designing more suitable catalyst for environmental protection.

## Acknowledgments

This project is supported by special fund of State Key Joint Laboratory of Environment Simulation and Pollution Control (17K08ESPCT), National Natural Science Foundation of China (21677083, 21707107) and Suzhou-Tsinghua innovation guiding program (No. 2016SZ0104).

## Appendix A. Supplementary data

Supplementary data associated with this article can be found, in the online version, at <http://dx.doi.org/10.1016/j.apcatb.2017.11.019>.

## References

- [1] T. Salthammer, S. Mentese, R. Marutzky, Formaldehyde in the indoor environment, *Chem. Rev.* 110 (2010) 2536–2572.
- [2] T. Salthammer, Formaldehyde in the ambient atmosphere: from an indoor pollutant to an outdoor pollutant, *Angew. Chem. Int. Ed.* 52 (2013) 3320–3327.
- [3] L. Zhu, D.J. Jacob, F.N. Keutsch, L.J. Mickley, R. Scheffé, M. Strum, G.G. Abad, K. Chance, K. Yang, B. Rappenglück, D.B. Millet, M. Baasandorj, L. Jaegle, V. Shah, Formaldehyde (HCHO) as a hazardous air pollutant: mapping surface air concentrations from satellite and inferring cancer risks in the United States, *Environ. Sci. Technol.* 51 (2017) 5650–5657.
- [4] J. Ye, X. Zhu, B. Cheng, J. Yu, C. Jiang, Few-layered graphene-like boron nitride: a highly efficient adsorbent for indoor formaldehyde removal, *Environ. Sci. Technol. Lett.* 4 (2017) 20–25.
- [5] C. Zhang, H. He, K. Tanaka, Perfect catalytic oxidation of formaldehyde over a Pt/TiO<sub>2</sub> catalyst at room temperature, *Catal. Commun.* 6 (2005) 211–214.
- [6] H. Huang, D.Y.C. Leung, Complete elimination of indoor formaldehyde over supported Pt catalysts with extremely low Pt content at ambient temperature, *J. Catal.* 280 (2011) 60–67.
- [7] C. Zhang, F. Liu, Y. Zhai, H. Ariga, N. Yi, Y. Liu, K. Asakura, M.F. Stephanopoulos, H. He, Alkali-metal-promoted Pt/TiO<sub>2</sub> opens a more efficient pathway to formaldehyde oxidation at ambient temperatures, *Angew. Chem. Int. Ed.* 51 (2012) 9628–9632.
- [8] L. Nie, J. Yu, X. Li, B. Cheng, G. Liu, M. Jaroniec, Enhanced performance of NaOH-modified Pt/TiO<sub>2</sub> toward room temperature selective oxidation of formaldehyde, *Environ. Sci. Technol.* 47 (2013) 2777–2783.
- [9] X. Zhu, B. Cheng, J. Yu, W. Ho, Halogen poisoning effect of Pt-TiO<sub>2</sub> for formaldehyde catalytic oxidation performance at room temperature, *Appl. Surf. Sci.* 364 (2016) 808–814.
- [10] Y. Li, C. Zhang, J. Ma, M. Chen, H. Deng, H. He, High temperature reduction dramatically promotes Pd/TiO<sub>2</sub> catalyst for ambient formaldehyde oxidation, *Appl. Catal. B: Environ.* (2017), <http://dx.doi.org/10.1016/j.apcatb.2017.06.023>.
- [11] Y. Ma, G. Zhang, Sepiolite nanofiber-supported platinum nanoparticle catalysts toward the catalytic oxidation of formaldehyde at ambient temperature: efficient and stable performance and mechanism, *Chem. Eng. J.* 288 (2016) 70–78.
- [12] Z. Yan, Z. Xu, B. Cheng, C. Jiang, Co<sub>3</sub>O<sub>4</sub> nanorod-supported Pt with enhanced performance for catalytic HCHO oxidation at room temperature, *Appl. Surf. Sci.* 404 (2017) 426–434.
- [13] Z. Yan, Z. Xu, J. Yu, M. Jaroniec, Highly active mesoporous ferrihydrite supported Pt catalyst for formaldehyde removal at room temperature, *Environ. Sci. Technol.* 49 (2015) 6637–6644.
- [14] S.J. Park, I. Bae, I.S. Nam, B.K. Cho, S.M. Jung, J.H. Lee, Oxidation of formaldehyde over Pd/Beta catalyst, *Chem. Eng. J.* 195 (2012) 392–402.
- [15] C. Zhang, Y. Li, Y. Wang, H. He, Sodium-promoted Pd/TiO<sub>2</sub> for catalytic oxidation of formaldehyde at ambient temperature, *Environ. Sci. Technol.* 48 (2014) 5816–5822.
- [16] H. Tan, J. Wang, S. Yu, K. Zhou, Support morphology-dependent catalytic activity of Pd/CeO<sub>2</sub> for formaldehyde oxidation, *Environ. Sci. Technol.* 49 (2015) 8675–8682.
- [17] Q. Xu, W. Lei, X. Li, X. Qi, J. Yu, G. Liu, J. Wang, P. Zhang, Efficient removal of formaldehyde by nanosized gold on well-defined CeO<sub>2</sub> nanorods at room temperature, *Environ. Sci. Technol.* 48 (2014) 9702–9708.
- [18] B. Chen, X. Zhu, M. Crocker, Y. Wang, C. Shi, FeO<sub>x</sub>-supported gold catalysts for catalytic removal of formaldehyde at room temperature, *Appl. Catal. B: Environ.* 154 (2014) 73–81.
- [19] C. Ma, G. Pang, G. He, Y. Li, C. He, Z. Hao, Layered sphere-shaped TiO<sub>2</sub> capped with gold nanoparticles on structural defects and their catalysis of formaldehyde oxidation, *J. Environ. Sci.* 29 (2016) 77–85.
- [20] P. Hu, Z. Amghouz, Z. Huang, F. Xu, Y. Chen, X. Tang, Surface-Confined atomic silver centers catalyzing formaldehyde oxidation, *Environ. Sci. Technol.* 49 (2015) 2384–2390.
- [21] Y. Chen, Z. Huang, M. Zhou, Z. Ma, J. Chen, X. Tang, Single silver adatoms on nanostructured manganese oxide surfaces: boosting oxygen activation for benzene abatement, *Environ. Sci. Technol.* 51 (2017) 2304–2311.
- [22] B. Bai, Q. Qiao, H. Arandian, J. Li, J. Hao, Three-Dimensional ordered mesoporous MnO<sub>2</sub>-Supported Ag nanoparticles for catalytic removal of formaldehyde, *Environ. Sci. Technol.* 50 (2016) 2635–2640.
- [23] D. Li, G. Yang, P. Li, J. Wang, P. Zhang, Promotion of formaldehyde oxidation over Ag catalyst by Fe doped MnO<sub>x</sub> support at room temperature, *Catal. Today* 277 (2016) 257–265.
- [24] Y. Huang, B. Long, M. Tang, Z. Rui, M.S. Balogun, Y. Tong, H. Ji, Bifunctional catalytic material: an ultrastable and high-performance surface defect CeO<sub>2</sub> nanosheets for formaldehyde thermal oxidation and photocatalytic oxidation, *Appl. Catal. B: Environ.* 181 (2016) 779–787.
- [25] P. Liu, H. He, G. Wei, X. Liang, F. Qi, F. Tan, W. Tan, J. Zhu, R. Zhu, Effect of Mn substitution on the promoted formaldehyde oxidation over spinel ferrite: catalyst characterization, performance and reaction mechanism, *Appl. Catal. B: Environ.* 182 (2016) 476–484.
- [26] Z. Wang, W. Wang, L. Zhang, D. Jiang, Surface oxygen vacancies on Co<sub>3</sub>O<sub>4</sub> mediated catalytic formaldehyde oxidation at room temperature, *Catal. Sci. Technol.* 6 (2016) 3845–3853.
- [27] Y. Sekine, Oxidative decomposition of formaldehyde by metal oxides at room temperature, *Atmos. Environ.* 36 (2002) 5543–5547.
- [28] R. Averlant, S. Royer, J.M. Giraudon, J.P. Bellat, I. Bezverkhyy, G. Weber, J.F. Lamonié, Mesoporous silic-confined manganese oxide nanoparticles as highly efficient catalysts for the low-temperature elimination of formaldehyde, *ChemCatChem* 6 (2014) 152–161.
- [29] M.A. Sidheswaran, H. Destaillets, D.P. Sullivan, J. Larsen, W.J. Fisk, Quantitative room temperature mineralization of airborne formaldehyde using manganese oxide catalysts, *Appl. Catal. B: Environ.* 107 (2011) 34–41.
- [30] J. Quiroz, J.M. Giraudon, A. Gervasini, C. Dujardin, C. Lancelot, M. Trentesaux, J.F. Lamonié, Total oxidation of formaldehyde over MnO<sub>x</sub>-CeO<sub>2</sub> catalysts: the effect of acid treatment, *ACS Catal.* 5 (2015) 2260–2269.
- [31] L. Zhu, J. Wang, S. Rong, H. Wang, P. Zhang, Cerium modified birnessite-type MnO<sub>2</sub> for gaseous formaldehyde oxidation at low temperature, *Appl. Catal. B: Environ.* 211 (2017) 212–221.
- [32] S. Selvakumar, N. Nuns, M. Trentesaux, V.S. Batra, J.M. Giraudona, J.F. Lamonié, Reaction of formaldehyde over birnessite catalyst: A combined XPS and ToF-SIMS study, *Appl. Catal. B: Environ.* (2017), <http://dx.doi.org/10.1016/j.apcatb.2017.05.029>.
- [33] L. Lu, H. Tian, J. He, Q. Yang, Graphene-MnO<sub>2</sub> hybrid nanostructure as a new catalyst for formaldehyde oxidation, *J. Phys. Chem. C* 120 (2016) 23660–23668.
- [34] J. Zhou, L. Qin, W. Xiao, C. Zeng, N. Li, T. Lv, H. Zhu, Oriented growth of layered-MnO<sub>2</sub> nanosheets over α-MnO<sub>2</sub> nanotubes for enhanced room-temperature, *Appl. Catal. B: Environ.* 207 (2017) 233–243.
- [35] J. Wang, R. Yunus, J. Li, P. Li, P. Zhang, J. Kim, In situ synthesis of manganese oxides on polyester fiber for formaldehyde decomposition at room temperature, *Appl. Surf. Sci.* 357 (2015) 787–794.
- [36] J. Wang, G. Zhang, P. Zhang, Layered birnessite-type MnO<sub>2</sub> with surface pits for enhanced catalytic formaldehyde oxidation activity, *J. Mater. Chem. A* 5 (2017) 5719–5725.
- [37] J. Zhang, Y. Li, L. Wang, C. Zhang, H. He, Catalytic oxidation of formaldehyde over manganese oxides with different crystal structures, *Catal. Sci. Technol.* 5 (2015) 2305–2313.
- [38] J. Wang, P. Zhang, J. Li, C. Jiang, G. Yunus, J. Kim, Room-temperature oxidation of formaldehyde by layered manganese oxide: effect of water, *Environ. Sci. Technol.* 49 (2015) 12372–12379.
- [39] J. Wang, J. Li, C. Jiang, P. Zhou, P. Zhang, J. Yu, The effect of manganese vacancy in birnessite-type MnO<sub>2</sub> on room-temperature oxidation of formaldehyde in air, *Appl. Catal. B* 204 (2017) 147–155.
- [40] S. Rong, P. Zhang, Y. Yang, L. Zhu, J. Wang, F. Liu, MnO<sub>2</sub> framework for instantaneous mineralization of carcinogenic airborne formaldehyde at room temperature, *ACS Catal.* 7 (2017) 1057–1067.
- [41] J. Hou, L. Liu, Y. Li, M. Mao, H. Lv, X. Zhao, Tuning the K<sup>+</sup> Concentration in the tunnel of OMS-2 nanorods leads to a significant enhancement of the catalytic activity for benzene oxidation, *Environ. Sci. Technol.* 47 (2013) 13730–13736.
- [42] Y. Chen, J. Gao, Z. Huang, M. Zhou, J. Chen, C. Li, Z. Ma, J. Chen, X. Tang, Sodium rivals silver as single-atom active centers for catalyzing abatement of formaldehyde, *Environ. Sci. Technol.* 51 (2017) 7084–7090, <http://dx.doi.org/10.1021/acs.est.7b00499>.
- [43] F. Xu, Z. Huang, P. Hu, Y. Chen, L. Zheng, J. Gao, X. Tang, The promotion effect of isolated potassium atoms with hybridized orbitals in catalytic oxidation, *Chem. Commun.* 51 (2015) 9888–9891.
- [44] B. Bai, J. Li, Positive effects of K<sup>+</sup> ions on three-dimensional mesoporous Ag/Co<sub>3</sub>O<sub>4</sub> catalyst for HCHO oxidation, *ACS Catal.* 4 (2014) 2753–2762.
- [45] Y. Zhai, D. Pierre, R. Si, W. Deng, P. Ferrin, A.U. Nilekar, G. Peng, J.A. Herron, D.C. Bell, H. Saltsburg, M. Mavrikakis, M. Flytzani-Stephanopoulos, Alkali-stabilized Pt-OH<sub>x</sub> species catalyze low-temperature water-gas shift reactions, *Science* 329 (2010) 1633–1636.
- [46] J. Jia, P. Zhang, L. Chen, Catalytic decomposition of gaseous ozone over manganese dioxide with different crystal structures, *Appl. Catal. B: Environ.* 189 (2016) 210–218.
- [47] C. Julien, M. Massot, R. Baddour-Hadjean, S. Franger, S. Bach, J.P. Pereira-Ramos, Raman spectra of birnessite manganese dioxides, *Solid State Ion.* 159 (2003) 345–356.
- [48] H. Wu, W. Cai, M. Long, H. Wang, Z. Wang, C. Chen, X. Hu, X. Yu, Sulfur dioxide capture by heterogeneous oxidation on hydroxylated manganese dioxide, *Environ. Sci. Technol.* 50 (2016) 5809–5816.
- [49] D. Widmann, R.J. Behm, Activation of molecular oxygen and the nature of the active oxygen species for CO oxidation on oxide supported Au catalysts, *Acc. Chem. Res.* 47 (2014) 740–749.
- [50] P. Mars, D.W. Van Krevelen, Oxidations carried out by means of vanadium oxide catalysts, *Chem. Eng. Sci.* 3 (1954) 41–59.